Supplementary Information (SI) for Nanoscale Horizons.
This journal is © The Royal Society of Chemistry 2025

Supplement

Creating Chirality in WSe_2 Through Screw Dislocation by Chemical Vapor Transport

Authors: Philip Putze[1], Tobias Ritschel[2], Paul Chekhonin[3], Jochen Geck[2], Daniel Wolf[1], Alexey A. Popov[1], Bernd Büchner[1,2], Peer Schmidt[4], Silke Hampel[1]**

[1]Leibniz Institute for Solid State and Materials Research, Institute for Solid State Research, Helmholtzstraße 20, 01069 Dresden, Germany

[2]Institute of Solid State and Materials Physics, Department of Physics, TUD Dresden University of Technology, Haeckelstraße 3, 01069 Dresden, Germany

[3]Helmholtz-Zentrum Dresden-Rossendorf, Institute of Resource Ecology, Bautzner Landstraße 400, 01328 Dresden, Germany

[4]Brandenburg University of Technology (BTU) Cottbus - Senftenberg, Chair of Inorganic Chemistry, Universitätsplatz 1, 01968 Senftenberg, Germany

KEYWORDS: Chiral WSe_2, Twisted nanostructures, Screw dislocation, Synthesis, Transition metal dichalcogenides, Chemical Vapor Transport, 2D materials, Thermodynamic Simulation.

Work-up for the Chemical Vapor Transport Process

Preparation of the Substrates

Si(100) substrates (Alfa Aesar; single-polished, p-typ, B-doped) were used with dimensions of 5.0 mm × 3.3 mm × 0.25 mm ($L \times W \times H$). SiO_2 nanoparticles (Sigma Aldrich, 99.8 %) with a diameter of $d(SiO_2) \approx 200$ nm were diluted in ethanol. Two drops of the solution with $\omega(SiO_2) = 0.30$ mg·mL^{-1} were deposited by the dropcast and spin coating method. Substrates were treated at elevated temperature in a CWF 1200 Chamber Furnace (Carbolite Gero) with specific heating rates, see Table **S 1**. The temperature target was 1200 °C with a dwell time of $t_{\mathrm{dwell}} = 6$ h.

Table S 1. Specific heating rates for the thermal treatment of the SiO_2@Si(100) substrates.

ϑ / °C	β / K·min^{-1}
600	25
800	15
1000	10
1100	5
> 1100	3

For characterization of the nanoparticles, SEM and AFM were utilized. Various substrate areas were depicted to ensure the substrate is covered with SiO_2 nanoparticles, see Figure **S 1** a-f). Specific height profiles based on AFM measurements are depicted in Figure **S 1** g-i).

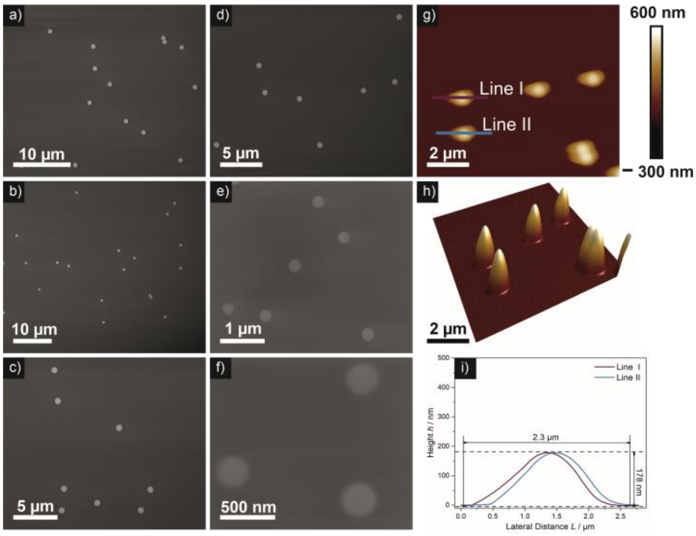

Figure S 1. Characterization of SiO_2@Si(100) substrates. a-f) SEM images in varying magnification to highlight the well-distrubuted SiO_2 nanoparticles seeded on the substrate. g) AFM height profile images of a selected area on the substrate. h) 3D AFM image of the same substrate area (color code is according to g)). i) Height profile of two selected nanoparticles indicating the suface-fused character and a height of around 178 nm.

Thermodynamic Data

Datasets used for modelling consist of values for the standard enthalpy of formation $\Delta_{\mathrm{B}}\overset{\circ}{H}_T$, standard entropy $\overset{\circ}{S}_T$, parameters for a molar heat capacity function $C_{\mathrm{p}}(T)$ and the temperature which the other values referring to. The values of the variables *a*, *b*, *c*, …, *g* are specified as coefficients of the C_{p}-function, as described by eq. (**S1**). The whole dataset is implemented into the TRAGMIN program [1] exactly as it is denoted in Table **S 2**.

$$C_p(T) = a + b \cdot 10^{-3} T + c \cdot 10^{6} T^{-2} + d \cdot 10^{-6} T^{2} + e \cdot 10^{5} T^{3} + f \cdot 10^{4} T^{-0.5} + g \cdot 10^{-1} T^{0.5} \qquad \text{(S1)}$$

Table S 2. Allocation of the thermodynamic data used for calculations *via* TRAGMIN [1].

			$C_p(T)$ / J·mol^{-1}·K^{-1}								
Species	$\Delta_{\mathrm{B}}H^{\circ}_T$ / J·mol^{-1}	S°_T / J·mol^{-1}·K^{-1}	a	$b \cdot 10^{-3}$	$c \cdot 10^{6}$	$d \cdot 10^{-6}$	$e \cdot 10^{5}$	$f \cdot 10^{4}$	$g \cdot 10^{-1}$	T / K	**Ref.**
Ar(g)	0	154.845	20.786							298	2
Cl(g)	121,302	165.189	26.529	3.103			− 0.011			298	3
Cl(g)			24.067		− 1.753		0.093	− 0.028	− 0.137	600	3
Cl_2(g)	0	223.079	20.681		0.317		− 0.083	0.059	1.911	298	3
HCl(g)	− 92,312	186.901	13.384	1.731	0.623	− 3.803	0.053			298	3
Se(s)	0	42.258	17.891	25.104						298	2
Se(l)	11,278	68.029	35.146							493	2
Se(g)	235,350	176.715	21.464	1.506	− 0.092					298	2
Se_2(g)	136,699	243.618	44.601	− 2.657	− 0.251					298	2
Se_3(g)	173,518	315.038	58.145	3.038	− 0.222					298	2
Se_4(g)	180,631	379.204	83.082	0.033	− 0.251					298	2
Se_5(g)	135,444	385.359	107.926	0.088	− 0.590					298	2
Se_6(g)	132,515	433.613	132.905	0.067	− 0.594					298	2
Se_7(g)	141,302	486.474	157.762	0.113	− 0.828					298	2
Se_8(g)	152,176	531.159	182.740	0.092	− 0.494					298	2
$SeCl_2$(g)	− 33,472	295.708	57.948	0.134	− 0.393					298	2
Se_2Cl_2(g)	− 21,756	353.908	82.383	1.573	− 0.452					298	2
$SeCl_4$(s)	− 188,698	194.556	133.888							298	2
SeO(g)	− 62,341	233.994	34.936	1.506	− 0.368					298	2
SeO_2(g)	− 107,842	264.998	52.844	3.088	− 0.992					298	2
W(s)	0	32.660	24.493	2.741	− 0.079	0.167				298	2
WCl_2(s)	− 260,286	130.541	71.283	21.903						298	2
WCl_2(g)	− 12,552	309.407	58.166	4.506	− 0.100					298	2

			$C_p(T)$ / $\mathrm{J \cdot mol^{-1} \cdot K^{-1}}$								
Species	$\Delta_B H°_T$ / $\mathrm{J \cdot mol^{-1}}$	$S°_T$ / $\mathrm{J \cdot mol^{-1} \cdot K^{-1}}$	a	$b \cdot 10^{-3}$	$c \cdot 10^{6}$	$d \cdot 10^{-6}$	$e \cdot 10^{5}$	$f \cdot 10^{4}$	$g \cdot 10^{-1}$	T / K	**Ref.**
WCl_4(s)	− 443,085	198.322	113.449	54.601						298	2
WCl_4(g)	− 335,849	379.280	107.403	0.460	− 0.778					298	2
WCl_5(s)	− 513,021	217.568	124.449	109.922	− 0.142					298	2
WCl_5(g)	− 412,542	405.538	131.378	1.406	1.029					298	2
WCl_6(g)	− 493,611	419.325	157.544	0.188	− 1.226					298	2
WO_2(g)	76,567	285.495	52.133	3.690	− 0.837					298	2
WO_2Cl_2(s)	− 780,316	200.832	79.513	94.107	− 0.285					298	2
WO_2Cl_2(g)	− 671,498	353.929	103.575	2.301	− 1.573					298	2
WSe_2(s)	− 188,280	90.015	71.086	14.627	0.253					298	3

Calculation of the Vapor Pressure Behavior

Essential parameters, such as temperature and amount of starting material can be portrayed for the W/Se/Cl system for the temperature range 400 °C $\leq \vartheta \leq$ 1100 °C based on the stationary simulations according to the ternary phase diagram W/Se/Cl, see Figure **S 2** a-b). Modelling suggest that the co-existence phase ranges I and II do not allow dissolution and precipitation due to the low selenium activity, see Figure **S 2** b). Indeed, phase pure WSe_2(s) can be synthesized as precipitate when adding $SeCl_4$(s) as transport addition according to range III in the ternary phase diagram and the simulated CVT. Here, species of Se_2(g), WCl_4(g), and $SeCl_2$(g), Cl_2(g) and Se_3(g) with a lower partial pressure contribute, see Figure **S 2** c). Generally, only species with a partial pressure of $p_i > 10^{-5}$ bar affect the vapor transport to an estimable level [4]. Thus, gaseous species with a partial pressure of $p_i < 10^{-5}$ bar are non-effective. Phase range I indicates that WCl_2(s) undergoes both sublimation and decomposition, which leads to the formation of W(s) and WCl_4(s). The vapor pressure behavior of WCl_2(g) underlines the side reactions. In combination with the TRAGMIN simulations, all phases in the light blue-marked phase range I are condensed and are close to WSe_2(s). Regarding to phase range I, Se_2(g) builds up a relatively low vapor pressure and is only edge close to a reasonable transport efficiency. According to the simulations (Figure **S 2** b)), a proper temperature range is set from around 800 °C to 950 °C to meet the preconditions for a working CVT process. Selenium Se_2(g) becomes a transport-relevant species from around 950 °C. With the addition of $SeCl_4$(s), the activity of Se_2(g) is strongly enhanced and thus the partial pressures of the relevant species are sufficiently high. $SeCl_4$(s) can then be considered as practicable transport addition and essential to reach the dark blue-marked phase range III in the ternary phase diagram, and thus allowing a phase-pure precipitation of $WSe_2(s)$.

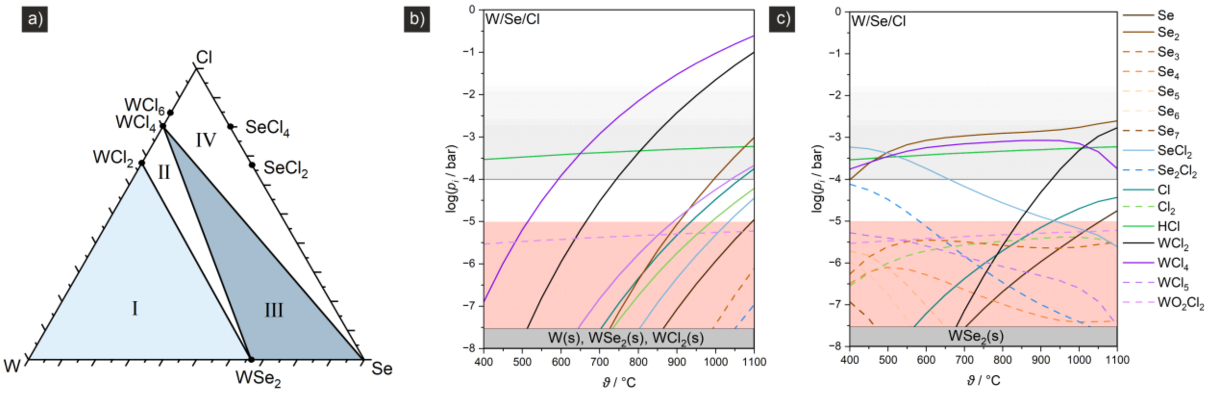

Figure S 2. a) Ternary phase diagram of W/Se/Cl at $T = 1133$ K and $p = 1$ bar. Phase ranges labeled: I: $W(s) + WCl_2(s) + WSe_2(s)$, II: $WCl_2(s) + WSe_2(s) + Cl(g)$, III: $WSe_2(s) + Cl(g)$, IV: Cl(g). b) Partial pressure for different gas species in the temperature range of $400\ °C \leq \vartheta \leq 1100\ °C$ for the stationary simulation according to phase range I in the ternary diagram. c) Partial pressures modelled for the stationary simulation according to phase range III. Area for $\log(p_i) > -4$ is marked grey. Non-effective pressure area for $p \leq 10^{-5}$ bar is marked red with species given as dashed line. Condensed phases given in dark grey rectangle.

Only the gaseous species with a partial pressure of $p_i \geq 10^{-5}$ bar contribute to an estimable level of vapor transport experiments [4]. Thus, gaseous species with lower partial pressures are non-effective. Modellings including a stoichiometric ratio of W:Se = 1:2.001 and 0.004 mmol Cl suggest that phase-pure $WSe_2(s)$ can be synthesized as precipitate. Large excess of Se (220 mmol) results in Se(l) as boundary phase, while one-room simulations with a negligible amount of Cl lead to additional boundary phases of W(s) and $WCl_2(s)$. The calculated vapor pressure behavior includes the homogeneous equilibria of the selenium species according to eq. (**S3**). Thus, the contribution of the selenium species is more complex and affects the initial transport efficiency of $Se_2(g)$ to a certain degree. However, $Se_2(g)$ is the dominant selenium species. Its transport efficiency is eventually corrected for the partial contributions of the homologous series of Se species. As a result, $Se_2(g)$ and $WCl_4(g)$ are transport effective, whereas negative values of the transport efficiency indicate species that take up the role as transport agent, which is dominantly $SeCl_2(g)$. In turn, quantities of transport efficiencies provide the ratio between the species and can be referred as to the stoichiometric ratios for the dominant transport reaction.

The partial pressures and the equilibrium constant refer thereby directly or indirectly to the partial pressures of the gaseous species which are determined by the modelling of the gaseous phase composition. Additionally, there is a homogeneous equilibrium including the disproportionation of Se_2Cl_2(g), forming Se_2(g) and $SeCl_2$(g). This concludes a formal dominating transport equation eq. (**1**). It is the transport addition of $SeCl_4$(s) that lead to the formation of other transport-effective species in the first step of the process, and finally $SeCl_2$(g) becomes the transport agent. In accordance to the calculated partial pressures, the transport efficiency $\omega_t(i)$ for each species was calculated for the temperature range given as described by eq. (**S2**).

$$\omega_t(i) = \Delta\left(\frac{p_{i,\,T}}{p_{\mathrm{Ar},\,T}}\right)_{\mathrm{source} \rightarrow \mathrm{sink}} = \left(\frac{p_{i,\,T_2}}{p_{\mathrm{Ar},\,T_2}}\right)_{\mathrm{source}} - \left(\frac{p_{i,\,T_1}}{p_{\mathrm{Ar},\,T_1}}\right)_{\mathrm{sink}} \tag{S2}$$

Here, $\omega_t(i)$ is the transport efficiency, p_{i,T_2} represents the partial pressure for a gaseous species for the source side, p_{i,T_1} the partial pressure on the sink side and $p_{\mathrm{Ar},T}$ is the partial pressure for argon as reference for both sides of the ampoule. Partial pressures for the species were calculated in the temperature range of 800 °C $\leq \vartheta \leq$ 850 °C.

Since the system is more complicated with the addition of $SeCl_4$(s) under experimental conditions, more profound understanding of the CVT process can be ensured by interpreting the system in the homogeneous gas phase: in the first step of heterogeneous equilibria $SeCl_4$(s) forms the actual transport agent $SeCl_2$(g). In a further equilibrium, WCl_4(g) builds up one of the highest partial pressures according to modellings. However, the contribution of the selenium species is more complex. The reason lies in additional homogeneous equilibria in the gas phase between the homologous series of selenium species following eq. (**S3**) with $w \in [1; 8]$.

$$\frac{w}{2}\,\mathrm{Se}_2(\mathrm{g}) \;=\; \mathrm{Se}_w(\mathrm{g}) \tag{S3}$$

Thus, these properties contribute to a certain degree and were compromised to the relative transport efficiency of Se_2(g). In the course of simplifying the complexity and to exemplify the contribution of each species for the formation of the target product WSe_2(s), the transport efficiency was calculated. Considering the selenium entities, partial contributions of all selenium species were used to calculate the relative transport efficiency ($\omega_{t,\mathrm{rel}}$) according to eq. (**S4**). Hence, the relative transport efficiency of Se_2(g) corrected for the partial contributions of the homologous series of Se species is obtained.

$$\omega_{t,\mathrm{rel}} \;=\; \omega_0 + \sum_{w=1}^{8} \frac{w}{2}\cdot\omega_{\mathrm{Se}_w} \tag{S4}$$

Here, ω_0 represents the initial value for the transport efficiency of Se_2(g) cumulated with the scaling factor containing the partial contributions of the selenium homologues ω_{Se_w}. Selenium species with a positive value are transport effective, while species with a negative value are representatives for transport agents. $SeCl_2(g)$ and $Se_2Cl_2(g)$ are two entities exhibiting negative transport efficiencies and are expected to be formed. Entities without transport efficiency do not contribute to the formation of the crystals. Additionally to the single dominant transport reaction, the homogeneous reaction of the formed $Se_2Cl_2(g)$ is suggested by eq. (**S5**). Calculated transport efficiencies provide the ratio between tungsten tetrachloride and selenium as $WCl_4(s){:}Se_2(s) = 1{:}2$, while the ratio between selenium and selenium dichloride is $Se_2(s){:}SeCl_2(s) = 1{:}1$. This underlines that $WCl_4(g)$ and $Se_2(g)$ are transport-effective species and consumed during the CVT, whereas $SeCl_2(g)$ takes the role of the transport agent.

$$2\,\mathrm{Se_2Cl_2(g)} \rightleftharpoons 2\,\mathrm{SeCl_2(g)} + \mathrm{Se_2(g)} \tag{S5}$$

For the W:Se system, the transport rate $\dot{m}$ was calculated to be $\dot{m} = 2.15\ \mathrm{mg \cdot h^{-1}}$. It can be visualized appropriately in the course of the K_p of the dominant transport reaction. The range above $K_p = 10^{-4}$ characterizes the transport-effective temperature region, where values of low K_p represent low values of ΔK_p, too, while higher values of K_p allow a higher difference ΔK_p, see Figure **S 3**.

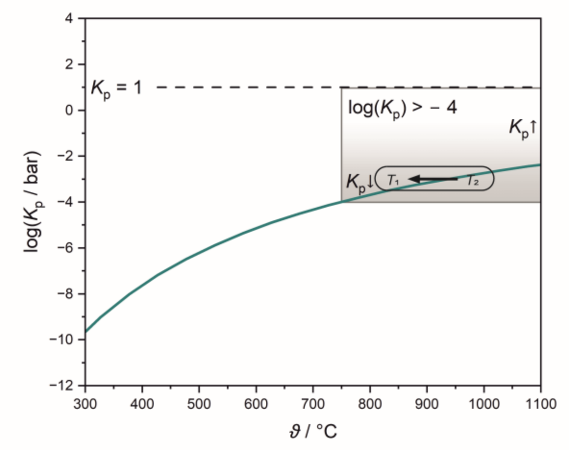

Figure S 3. Calculated equilibrium constant log(K_p / bar) over a wide temperature range ϑ /°C for the single dominant transport reaction. Grey rectangle shows a potential working window for the CVT. Schematic ampoule illustrates a position chosen for the experiment, where source (T_2) and sink (T_1) side are placed along the temperature gradient.

Bulk-WSe_2 was simulated accordingly, see Figure **S 4**a-b).

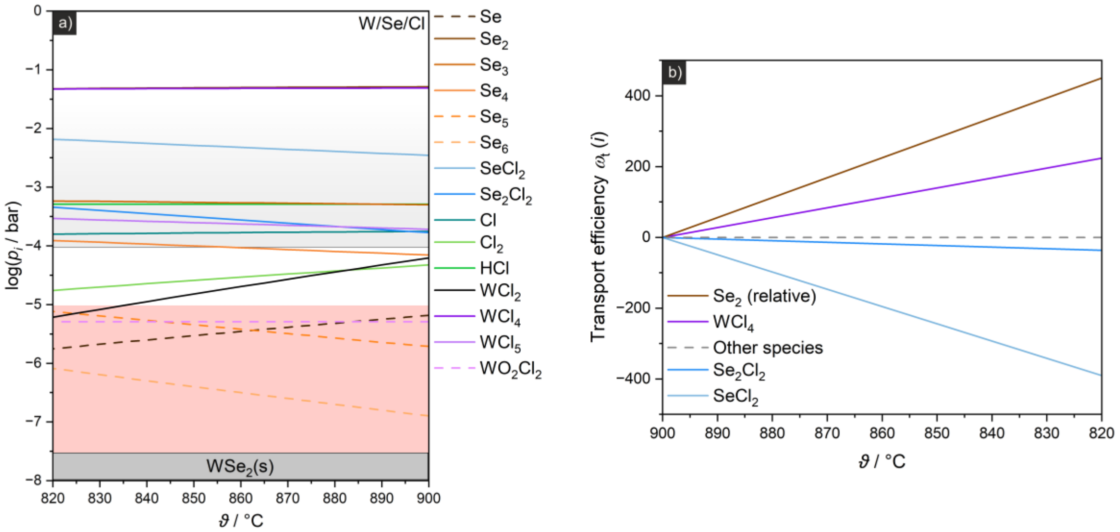

Figure S 4. Simulation of the partial pressure behavior in a sealed ampoule. a) Partial pressure for different gas species in the temperature range of 820 °C $\leq \vartheta \leq$ 900 °C for an endothermic CVT. Area for $\log(p_i) > -4$ is marked grey. Non-effective pressure area for $p \leq 10^{-5}$ bar is marked red with species given as dashed line. Condensed phases given in dark grey rectangle. b) Calculated transport efficiency $\omega_t(i)$ for the temperature range given. $\omega_{t,rel}(Se_2)$ corresponds to the homogeneous equilibria in the gas phase for Se_w species.

Table S 3. Essential CVT parameters for bulk-WSe_2 as simulated by TRAGMIN. One-room modelling represent the partial pressure over the source.

	***n*(*i*) / mmol**						
Modell	**W**	**Se**	**Cl**	**T_2 / °C**	**T_1 / °C**	**$\dot{m}_{calc.}$ / mg·h^{-1}**	**Boundary phases**
one room	100	220	0.0001	1100	400		Se(l)
one room	100	199.5	0.5	1100	400		W(s), WCl_2(s)
one room	1	2.001	0.0004	1100	400		-

pXRD data for bulk-WSe_2

pXRD reveals phase-pure bulk-WSe_2 was synthesized, see Table **S 4**. At this, the diffraction pattern is in accordance with the 2H structure type (ICSD: 40752, space group: $P6_3/mmc$)[5].

Table S 4. pXRD characterization for bulk-WSe_2 including the diffraction angle (2θ / °), the Miller indeces ($h\ k\ l$) and relative intensity ($I_{rel.}$ / a.u.) for each reflex.

2θ / °	**($h\ k\ l$)**	**$I_{rel.}$ / a.u.**
15.8	002	36.45
36.6	100	100.00
37.5	101	21.70
40.2	102	9.87
44.2	103	16.37
55.6	105	5.33
65.9	110	30.20
68.3	112	10.30
77.9	200	9.04
78.4	201	3.04
80.1	202	3.77
82.9	203	8.48
86.3	116	2.36
91.6	205	3.36
101.6	118	4.66
110.4	1011	2.97
112.5	211	5.23
117.8	213	1.24

EDX Spectra for nano-WSe_2

Representative EDX analysis from as-grown WSe_2 crystals with screw dislocation is given by Figure **S 5** a-b). The analysis gives strong evidence that the crystals were synthesized in a stoichiometric ratio of the elements of W:Se = 1:2.

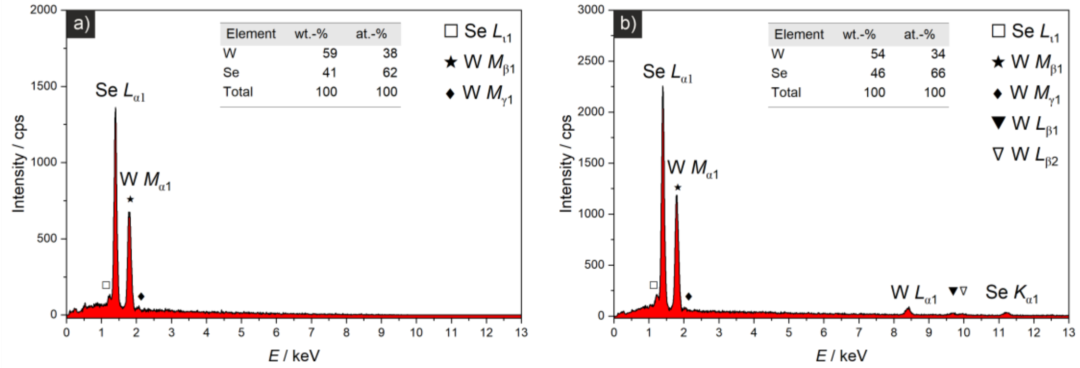

a)

Element	wt.-%	at.-%
W	59	38
Se	41	62
Total	100	100

b)

Element	wt.-%	at.-%
W	54	34
Se	46	66
Total	100	100

Figure S 5. EDX analysis of as-grown WSe_2 nanostructures with screw dislocation confirming the elemental ratio of W:Se = 1:2. a-b) EDX spectra correspond to the crystals depicted in Figure 4 a-b). Additional electron transitions for each element are labeled accordingly in the spectra.

Height Profile Data of Screwed WSe_2

All characteristic step heights and terrace widths obtained by AFM are enlisted in Table **S 5**. With these data, the respective slopes were calculated.

Table S 5. Obtained heights h / nm and terrace widths w / nm for the steps obtained on the WSe_2 crystals that were used to calculate the slope s. Growth conditions refer to the source and sink side of the ampoule.

Growth conditions	**Feature**	***h* / nm**	***w* / nm**	**Slope *s***
850 °C → 800 °C	1	32.3	812	0.0398
	2	16.2	538	0.0301
	3	12.9	484	0.0267
	4	12.0	493	0.0243
850 °C → 800 °C	1	9.8	637	0.0154
	2	10.3	707	0.0146
	3	10.0	676	0.0148
	3’	11.6	711	0.0163
	2’	10.3	711	0.0145
	1’	11.5	640	0.0180

Growth conditions	**Feature**	***h* / nm**	***w* / nm**	**Slope *s***
890 °C → 840 °C	1	28.9	601	0.0481
	2	16.6	374	0.0444
	3	15.8	249	0.0635
	4	9.8	528	0.0186
	5	16.8	300	0.0560
890 °C → 840 °C	1	5.3	534	0.0099
	2	5.5	520	0.0106
	3	5.2	342	0.0152
	4	3.2	278	0.0115
890 °C → 840 °C	1	8.1	418	0.0194
	2	7.6	551	0.0138
	3	6.3	152	0.0414
	4	6.4	475	0.0135
	5	6.8	551	0.0123
	6	8.1	475	0.0171
	7	6.3	323	0.0195
915 °C → 860 °C	1	3.6	160	0.0225
	2	2.8	104	0.0269
	3	2.1	164	0.0128
	4	1.2	219	0.0055
	5	3.3	104	0.0317
915 °C → 860 °C	1	5.6	393	0.0142
	2	4.8	140	0.0343
	3	4.7	201	0.0234
	4	3.9	210	0.0186
	5	3.1	175	0.0177

EBSD Evaluation

Representative EBSD pattern for the 2H-WSe_2 crystal allowed a direct comparison along the horizontal and vertical with respect to the orientation of the crystals. The whole crystal was mapped and chosen EBSD pattern analyzed with respect to the pattern shift according to the [001] zone axis, see Figure **S 6**.

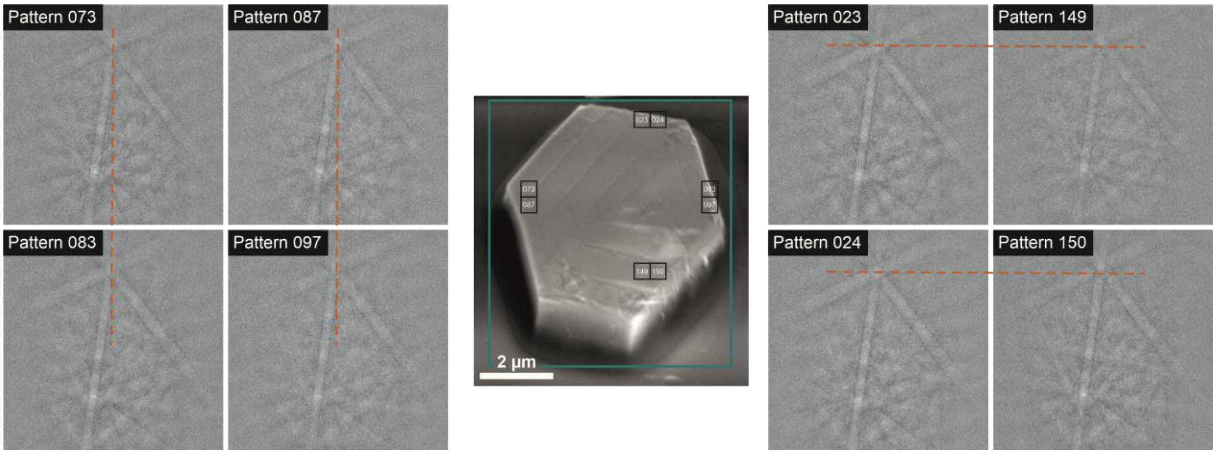

Figure S 6. EBSD pattern for selected areas of the EBSD mapping (solid green line) for direct comparison between horizontal and vertical pattern shifts of 2H-WSe_2. Dashed orange lines indicate pattern shift. Denoted pattern numbers correspond to locations within the schematic illustration of the mapping.

Vibrational Spectroscopy: Raman

In order to determine the best excitation source to obtain whether differences are given between the nm-scale WSe_2 and the bulk counterpart, three different lasers were applied. The excitation sources were $\lambda_{ex.}$ = 532 nm, $\lambda_{ex.}$ = 660 nm and $\lambda_{ex.}$ = 785 nm. Generally, the main Raman modes for WSe_2 were observed for both samples. However, the B^{1}_{2g} Raman mode for bulk-WSe_2 that is in association with vibrations between the WSe_2 layers was not observed with the 660 nm laser [6,7]. The broad Raman mode was observed with an excitation source of $\lambda_{ex.}$ = 532 nm, see Figure **S 7**. The decision on what excitation source suits best for our purpose, we specifically looked towards the 2 LA(M), $A_{1g}(M)$ and $E^{1}_{2g}(\Gamma)$ Raman modes. Thereby, the 2 LA(M) feature as shoulder was best visible with the 660 nm laser.

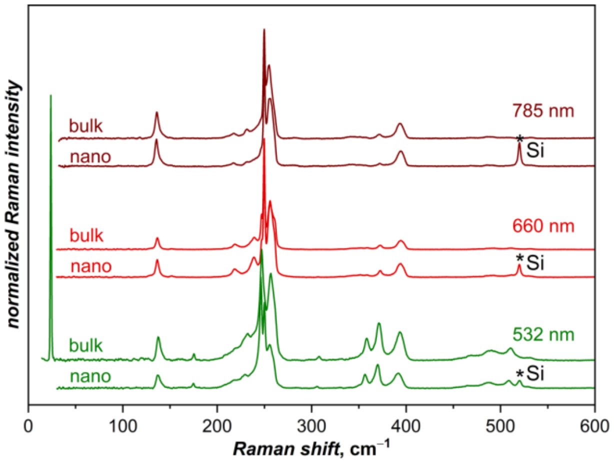

Figure S 7. Raman spectra of bulk and nano-WSe_2 excited with 785, 660, and 532 nm lasers.

Additional information about the Raman measurements are given by Figure S **8**.

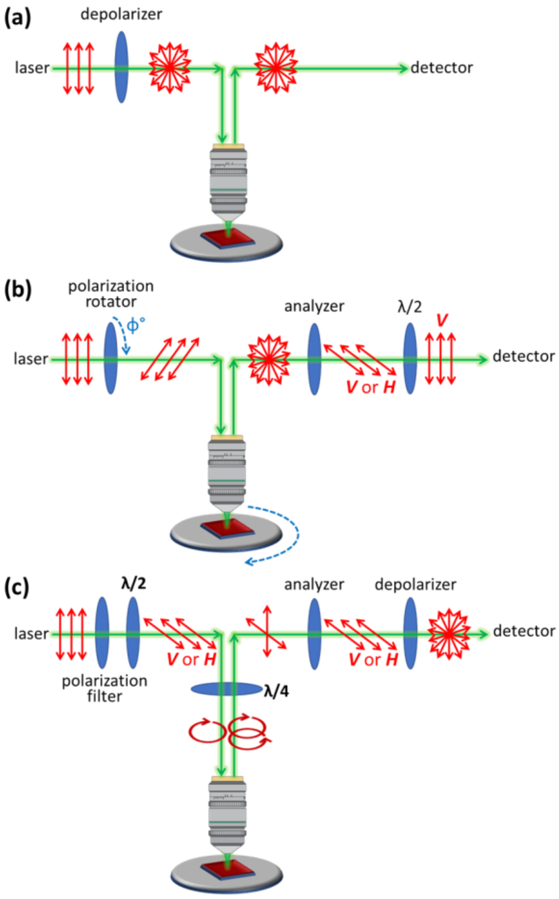

Figure S 8. Scheme of the optical elements used in Raman measurements. a) ***Non-polarized*** measurements: as the excitation laser has high degree of polarization (~100:1), the spectra of crystals will be affected by polarization. To avoid undesired polarization effects, we used polarization scrambler to depolarize the laser. b) ***Linear polarization***: polarization rotator was installed to rotate polarization plane of the laser at the required angle before entering objective. Scattered light was passed through analyzer to obtain vertical or horizontal linear polarized components. Since 1800 gratings are strongly sensitive to polarization of the incoming light (which results in different sensitivity for vertical and horizontal polarization), horizontallyoriented polarized light after analyzer was rotated to the vertical orientation using $\lambda/2$ plate. This way, gratings/CCD were always measuring light with vertically-oriented polarization, independently on the orientation after analyzer. c) ***Circular polarization***: polarization of the laser was first cleaned to 1000:1 degree using polarization filter, then laser was passed through $\lambda/2$ plate to rotate polarization plane, if necessary, by 90°. Right before objective, $\lambda/4$ plate is mounted, which transforms linear-polarized light to circular-polarized light (and circular polarized light to linear-polarized). Orientation of the fast axis of the $\lambda/4$ plate was adjusted to match the orientation of the linear polarization, else it would produce elliptically-polarized light. Depending on the mutual orientation of polarization plane and the fast axis of $\lambda/4$ plate, either right-hand or left-hand circular polarization is obtained and then directed to the sample through the objective. Scattered light collected by the objective has contributions from both right-hand and left-hand circular-polarized components. When it passes through $\lambda/4$ plate, it gives superposition of vertical and horizontal linear polarized light. Contribution of each component is obtained after passing through analyzer. Thus, by rotating the polarization plane before l/4 plate we can chose between left-hand and right-hand polarization of the excitation, whereas by choosing vertical or horizontal orientation of the analyzer we can determine intensity of left-hand and right-hand circular polarization in the scattered light. Depolarizer was installed before detector to prevent different sensitivity of the gratings to vertical and horizontal orientation of linear-polarized light.

CP-Raman measurements were conducted on several spots on WSe_2, see Figure S **9** and Figure S **10**.

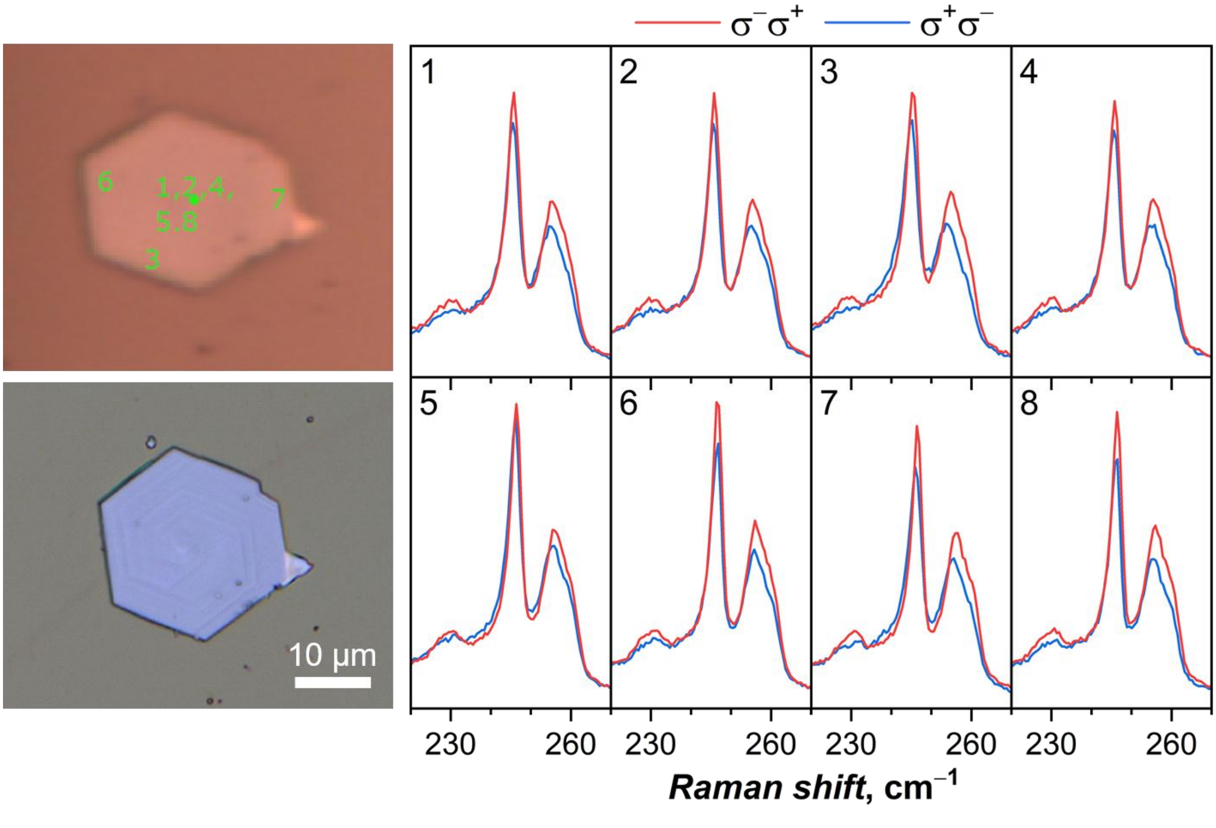

Figure S 9. Optical images of the crystal with right-hand chirality used in additional CP-Raman measurements. Green number on the optical image denote position of the laser spot, at which the spectra were acquired with $\sigma^+\sigma^-$ and $\sigma^-\sigma^+$ polarization. Spectra at different positions are shown in the 220-270 range, the most intense peak is of the E_{2g} mode, whereas A_{1g} mode is not active in $\sigma^+\sigma^-$ or $\sigma^-\sigma^+$ polarization.

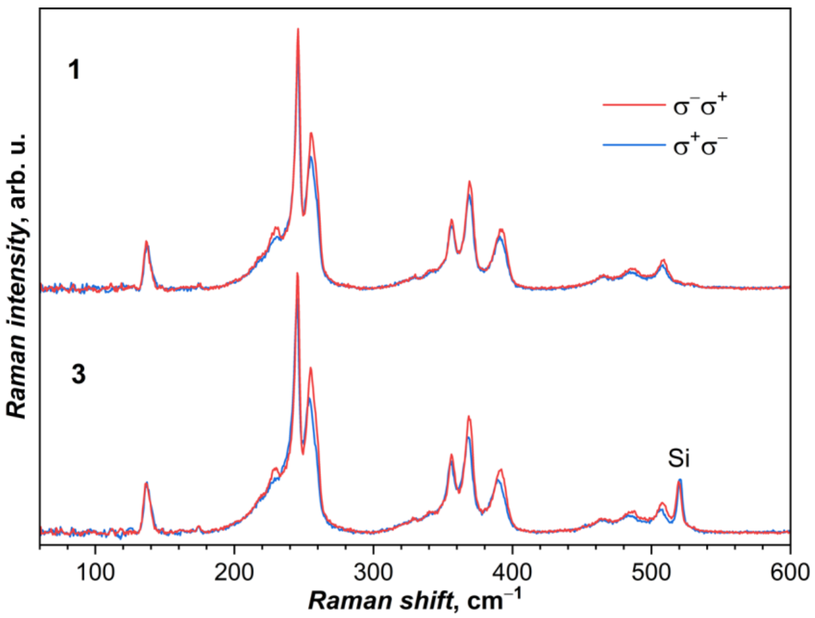

Figure S 10. Raman spectra measured at positions 1 and 3 with $\sigma^+\sigma^-$ and $\sigma^-\sigma^+$ polarization shown in a broader range. Note that since position 3 is close to the edge of the crystal, a fragment of the substrate was also illuminated by laser, giving the signal denoted as Si.

References

(1) G.Krabbes; W.Bieger; K.-H.Sommer; T.Söhnel; U.Steiner. GMIN Version 5.2: Package TRAGMIN for Calculation of Thermodynamic Equilibrium. Dresden 2014. https://www.htw-dresden.de/luc/forschung/chemieingenieurwesen/festkoerperchemie/tragmin.

(2) Knacke, O.; Kubaschewski, O. *Thermochemical Properties of Inorganic Substances*, 2nd ed.; Hesselmann, K., Ed.; Thermochemical Properties of Inorganic Substances; Stahleisen: Berlin Heidelberg, **1991**; pp 2412.

(3) Bale, C. W.; Bélisle, E.; Chartrand, P.; Decterov, S. A.; Eriksson, G.; Gheribi, A. E.; Hack, K.; Jung, I.-H.; Kang, Y.-B.; Melançon, J.; Pelton, A. D.; Petersen, S.; Robelin, C.; Sangster, J.; Spencer, P.; Van Ende, M.-A. FactSage Thermochemical Software and Databases, 2010–2016. *CALPHAD Comput. Coupling Phase Diagrams Thermochem.* **2016**, 54, 35–53. https://doi.org/10.1016/j.calphad.2016.05.002.

(4) Binnewies, M.; Glaum, R.; Schmidt, M.; Schmidt, P. *Chemical Vapor Transport Reactions*; Walter de Gruyter: Berlin/Bosten, **2012**; pp 25–26.

(5) Schutte, W. J.; De Boer, J. L.; Jellinek, F. Crystal Structures of Tungsten Disulfide and Diselenide. *J. Solid State Chem.* **1987**, 70 (2), 207–209. https://doi.org/10.1016/0022-4596(87)90057-0.

(6) Londoño-Calderon, A.; Dhall, R.; Ophus, C.; Schneider, M.; Wang, Y.; Dervishi, E.; Kang, H. S.; Lee, C.-H.; Yoo, J.; Pettes, M. T. Visualizing Grain Statistics in MOCVD WSe_2 through Four-Dimensional Scanning Transmission Electron Microscopy. *Nano Lett.* **2022**, 22 (6), 2578–2585. https://doi.org/10.1021/acs.nanolett.1c04315.

(7) O’Brien, M.; McEvoy, N.; Hanlon, D.; Hallam, T.; Coleman, J. N.; Duesberg, G. S. Mapping of Low-Frequency Raman Modes in CVD-Grown Transition Metal Dichalcogenides: Layer Number, Stacking Orientation and Resonant Effects. *Sci. Rep.* **2016**, 6 (1), 19476. https://doi.org/10.1038/srep19476.